

Molecular BioSystems

Accepted Manuscript



This is an *Accepted Manuscript*, which has been through the Royal Society of Chemistry peer review process and has been accepted for publication.

Accepted Manuscripts are published online shortly after acceptance, before technical editing, formatting and proof reading. Using this free service, authors can make their results available to the community, in citable form, before we publish the edited article. We will replace this *Accepted Manuscript* with the edited and formatted *Advance Article* as soon as it is available.

You can find more information about *Accepted Manuscripts* in the [Information for Authors](#).

Please note that technical editing may introduce minor changes to the text and/or graphics, which may alter content. The journal's standard [Terms & Conditions](#) and the [Ethical guidelines](#) still apply. In no event shall the Royal Society of Chemistry be held responsible for any errors or omissions in this *Accepted Manuscript* or any consequences arising from the use of any information it contains.



www.rsc.org/molecularbiosystems

ARTICLE

Molecular Modelling Studies of Sirtuin 2 Inhibitors Using Three-Dimensional Structure-Activity Relationship Analysis and Molecular Dynamics Simulations

Cite this: DOI: 10.1039/x0xx00000x

Received 00th January 2012,
Accepted 00th January 2012

DOI: 10.1039/x0xx00000x

www.rsc.org/

Yu-Chung Chuang,^a Ching-Hsun Chang,^a Jen-Tai Lin^b and Chia-Ning Yang^{†,a}

Sirtuin 2 (SIRT2) is a nicotinamide-adenine-dinucleotide-dependent histone deacetylase that plays a vital role in various biological processes related to DNA regulation, metabolism, and longevity. Recent studies on SIRT2 have indicated its therapeutic potential for neurodegenerative diseases such as Parkinson's disease. In this study, a series of SIRT2 inhibitors with a 2-anilinobenzamide core was analysed using a combination of molecular modelling techniques. A three-dimensional structure-activity relationship (3D-QSAR) model adopting comparative molecular field analysis (CoMFA) method with non-cross-validated correlation coefficient $R^2 = 0.992$ (for training set) and correlation coefficient $R_{test}^2 = 0.804$ (for test set) was generated to determine the structural requirements for inhibitory activity. Furthermore, we employed molecular dynamics (MD) simulations and the molecular mechanics/generalized Born surface area (MM/GBSA) method to compare the binding modes of a potent and selective compound interacting with SIRT1, SIRT2, and SIRT3 and also their binding free energies to shed light on the selectivity on the footing of structural and energetic investigation. The steric and electrostatic contour maps from the 3D-QSAR analysis identified several key interactions also observed in the MD simulations. According to these results, we provide guidelines for developing novel potent and selective SIRT2 inhibitors.

Introduction

The silent information regulator (SIR) protein family is highly conserved from bacteria to humans.¹⁻¹⁴ This protein family regulates gene silencing and is responsible for various biological functions and medical conditions, including cell-cycle regulation, cell survival, apoptosis, autophagy, inflammation, DNA recombination, DNA repair, glucose homeostasis, age-related diseases, diabetes, obesity, and neurodegenerative disorders.¹⁵⁻²⁶

In yeast, there are five SIR proteins (SIR1-5). SIR1-4 are essential for establishing and maintaining gene silencing. The SIR2-SIR3-SIR4 complex is involved in mating-type and telomeric silencing. SIRT2 interacting with other proteins is responsible for rDNA silencing.²⁷⁻³³ Seven sirtuin proteins have been reported in humans. Sirtuin 1 (SIRT1) is localized in the nucleus and modulates gene expression by deacetylating proteins, histone H4, p53, BCl6, and FOXO.^{12, 13, 18, 20, 23, 34-36} SIRT2 is localized in the cytoplasm and has been implicated in the process of cell division because it deacetylates α -tubulin.^{37, 38} SIRT3, SIRT4, and SIRT5 are mitochondrial proteins. SIRT3 has been demonstrated to be involved in the activation of

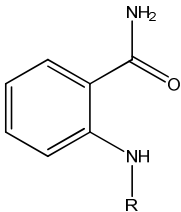
mitochondrial functions. SIRT4 was reported to play a regulatory role in the insulin secretion.³⁹⁻⁴¹ The function of SIRT5 remains unclear.³⁵ SIRT6 is localized in the nucleus and deacetylates lysine 9 of histone H3 in regulating telomeric metabolism and functions. SIRT7 is localized in the nucleus and is involved in the activation of RNA polymerase I transcription. Interestingly, only SIRT2 (Sirtulin) of all SIRT members is involved in gene-silencing methods from bacteria to higher eukaryotes. Therefore, the processes through which SIRT2 mediates gene silencing, the structure of SIRT2, and SIRT2 regulators (activators and inhibitors) have been widely studied in the previous decade.

In eukaryotic cells, gene silencing is regulated by histone deacetylases (HDACs). Four classes of zinc-dependent (classical) HDACs have been characterized: Class I (HDAC1, 2, 3, and 8), Class IIa (HDAC4, 5, 7, and 9), Class IIb (HDAC6 and 10), and Class IV (HDAC11). The nicotinamide adenine dinucleotide (NAD⁺)-dependent deacetylases are divided into two major groups, namely Class III or sirtuins, according to their mechanisms.^{22, 42-47} SIRT2 belongs to Class III deacetylase. During deacetylation, SIRT2 cleaves glycosidic

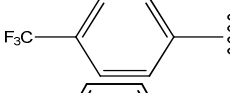
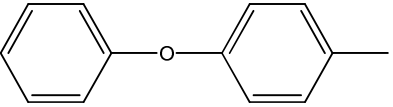
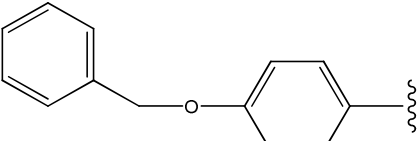
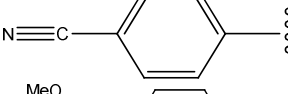
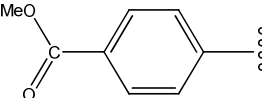
bonds and generates nicotinamide and the novel metabolite O-acetyl-ADP-ribose.²⁻⁵ Because SIRT2 has been proved to regulate various biological functions, the regulators of SIRT2 have potential therapeutic functions in cancer, HIV, obesity, diabetes, parkinsonian diseases, and Huntington disease.^{23, 26, 37, 48} Numerous potential SIRT2 inhibitors including the tryptamide-based TRIPOS 360702,^{49, 50} bisindolylmaleimide analogs,⁵¹ and

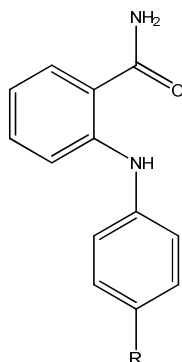
2-cyano-3-[5-(2,5-dichlorophenyl)-2-furanyl]-N-5-quinolinyl-2-propenamide²⁴ have been reported. Suzuki and colleagues recently synthesized and evaluated a novel series of 2-anilinobenzamide derivatives targeted at SIRT2 with the lowest IC₅₀ value of 0.57 μM (compound **39** as shown in Table 1).⁵² Moreover, **39** exhibited in vitro selectivity against SIRT1 (IC₅₀ > 300 μM) and SIRT3 (IC₅₀ > 300 μM) as evaluated by the same assay for compounds **1-46**.

Table 1. Chemical structures and IC₅₀ values of the 46 compounds used in developing QSAR models.⁵² (*Compounds in test set, whereas the other 29 compounds in training set.)



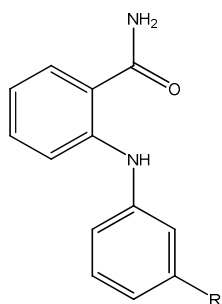
Compd. No.	Substituent (R)	IC ₅₀ (μM)
1	3-Ph-Ph	33
*2	3-Me-Ph	72
3	3-CF ₃ -Ph	100
4	3-OPh-Ph	25
*5	3-(E)-CH=CHCOOMe-Ph	32
6	3-CH ₂ CH ₂ COOMe-Ph	93

*7	4-Me-Ph		60
8	4-CF ₃ -Ph		69
*9	4-OMe-Ph		80
10	4-OBn-Ph		33
11	4-CN-Ph		93
12	4-COOMe-Ph		83



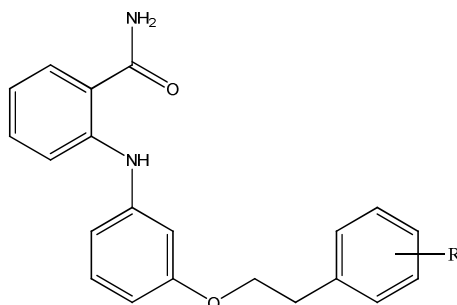
Compd. No.	Substituent (R)	IC ₅₀ (μM)
*13	(Z)-CH=CHPh	20
*14	CH ₂ CH ₂ Ph	88
15	CON(CH ₃)Ph	69
16	CONHPh	23

17	NHCOPh		17
18	NHCOCH ₃		77
*19	NHCOcyclohexyl		25
*20	NHCO-4-piperidinyl		53
*21	NHCO-3-Py		38



Compd. No.	Substituent (R)	IC ₅₀ (μM)
22	CONHPh	83
23	CONHCH ₂ Ph	39
24	CON(CH ₃)CH ₂ Ph	40
25	NHCOPh	57

26	NHCOCH ₂ Ph		74
27	OCH ₂ cyclohexyl		24
28	OCH ₂ CH(CH ₃) ₂		30
29	OCH ₂ Ph		54
*30	OCH ₂ CH ₂ CH ₂ Ph		4.3



Compd. No.	Substituent (R)	IC ₅₀ (μM)
*31	H	1.0
*32	2-CH ₃	1.8
33	3-CH ₃	1.8
34	4-CH ₃	1.6
*35	2-CF ₃	3.1
*36	3-CF ₃	2.1
37	4-CF ₃	1.4
*38	2-F	2.0
*39	3-F	0.57
40	4-F	2.7
41	2-Cl	1.5
42	3-Cl	2.0
43	4-Cl	0.83
44	2-Br	1.1
45	3-Br	3.4
*46	4-Br	1.2

Molecular dynamics (MD) simulation is a powerful tool in correlating protein structure and function because it enables elucidating protein structures and dynamics at the atomic level. Numerous researchers have used MD simulations in conjunction with experimental observations to investigate protein-protein and protein-small compound interactions.⁵³⁻⁵⁷ In addition, three-dimensional quantitative structure-activity

relationship (3D-QSAR) analysis adopting the comparative molecular field analysis (CoMFA) method⁵⁸ constitutes a computer-aided drug design approach for providing structural guidelines on small molecules and, regarding interactive fields, predicting the influence of activity. In this study, we applied 3D-QSAR analysis to obtain the structural requirements for drug development of SIRT2 inhibitors. MD simulations and

binding free-energy calculations using the molecular mechanics/generalized Born surface area (MM/GBSA) approach⁵⁹ were performed to evaluate the selectivity of **39** bound in SIRT1, SIRT2, and SIRT3. Compound **39** was investigated because, according to Suzuki and colleagues, who obtained an in vitro selectivity profile for SIRT1, SIRT2, and SIRT3, **39** exhibited a preference for SIRT2 over the other two SIRT proteins,⁵² regardless the 52% for SIRT2 vs. SIRT3 and 39% for SIRT2 vs. SIRT1 amino acid sequence similarity. The MD results for SIRT2-**39** were consistent with contour maps derived through 3D-QSAR analysis and were compared with SIRT1-**39** and SIRT3-**39** complexes predicted using the MD simulations. The conclusions drawn in this study provide insight into further structural modifications that yield more potent and selective SIRT2 inhibitors.

Computational Methods

Setup for CoMFA

Forty-six molecules and their inhibitory activities against SIRT2 were obtained from the data set designed and synthesized by Suzuki and colleagues.⁵² The structures and IC₅₀ values (μM) of these molecules against SIRT2 are listed in Table 1. We divided the 46 compounds into a training set containing 29 compounds for model generation and a test set containing 17 compounds (marked with an asterisk "*" in Table 1) for model validation. The test set compounds were selected according to the distribution of biological data and structural diversity, as indicated in Table 1 and Fig. 1. We chose the training and test set compounds based on random selection. For compounds 1–30 with higher structural diversity and a wider IC₅₀ values range (from 4.3 to 100 μM), we took a ratio of 2:1 for training and test set for compounds with a hope to use a larger training set to take all sorts of structural variation into consideration. However, because compounds 31–46 possess very minor structural differences on the substituent "R" in Table 1 and a narrow IC₅₀ range (between 0.57 and 3.4 μM), we took a ratio of nearly 1:1 when choosing the training set (9 compounds) and test set (7 compounds).

Alignment of the compounds is critical for determining a structure-activity relationship because discriminative inhibitory activities are firmly correlated with minor structural variations on a single corner of a series of compounds. We adopted a ligand-based approach for aligning the studied compounds because no cocrystal structure was available for SIRT2 bound with one of the studied inhibitors. All studied compounds were sketched and geometrically optimized in 5,000 steps by using Gasteiger-Hückel charge assignment, Tripos force-field parameters, and Powell method without constraints. The database alignment protocol in Sybyl 8.1⁶⁰ was used to align the structures according to the 2-anilinobenzamide core depicted in ball-and-stick representation as shown in Fig. 2. Two descriptors, including steric (Lennard-Jones 6-12 potential) and electrostatic (Coulombic potential) field energies, were calculated to build the CoMFA model by using an sp³-carbon atom, which carried a +1.0 charge and served as a probe atom placed at the lattice point of a region box. In the partial

least squares regression analysis, a leave-one-out (LOO) cross-validation was first performed to determine the optimal number of components (ONC). Further analysis with no cross-validation was then performed using the ONC to obtain the final QSAR model.

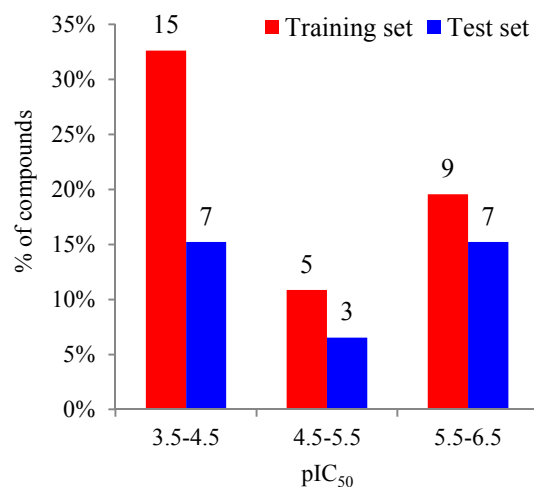


Fig. 1 Distribution of the inhibitory activities of the training set and test set compounds in the 3D-QSAR analysis. The number above each bar specifies the compound number in the corresponding pIC₅₀ range.

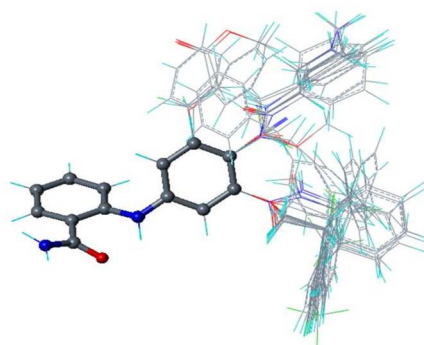


Fig. 2 Alignment of the 46 compounds in this study with the core structure specified in ball and stick presentation.

Setup for MD Simulations

The MD simulations were performed using AMBER 11.0 software package⁶¹ with ff03.r1⁶² and ff99SB force fields⁶³ to compare the binding modes of **39** in SIRT1, SIRT2, and SIRT3 and to explain the selectivity of **39**. X-ray crystallography revealed that the SIRT1 structure bound to NAD⁺ and the SIRT2 and SIRT3 structures bound to ADP ribose had the PDB codes 4I51,⁶⁴ 3ZGV,⁶⁵ and 4BN4,⁶⁶ respectively. The initial SIRT1-**39**, SIRT2-**39**, and SIRT3-**39** complex structures were generated after the removal of the bound ligand in each complex structure, although in the latter section it is demonstrated that the studied inhibitors take the substrate site instead of the NAD⁺ or ADP ribose site. The initial SIRT2-**39** complex structure was generated using the LibDock module in Discovery Studio 3.5⁶⁷ after consideration of the highest scored

pose of **39** in the highest scoring function. Because Suzuki and colleagues reported that the amide side chain of SIRT2 Q267 forms hydrogen bonds with the amino-hydrogen atom and the amide-oxygen atom in the 2-anilinobenzamide core,⁵² our docking simulations focused on a binding pocket including Q267. Fig. S1 (in supplementary material) shows the binding site sphere in SIRT2 set for the docking simulation where the amino acid residues were not allowed to adjust their orientations upon accommodating **39**. This highest scored pose of **39** according to the LibDock scoring function⁶⁸ (Table S1 in supplementary material) for this binding site was confirmed by our 3D-QSAR model; in other words, the spacious arrangement of the amino acids around **39** was consistent with the steric contour map generated using the CoMFA method. In addition, we applied a short MD simulation by using Discovery Studio 3.5⁶⁷ and employed the implicit water solvation setting on the LibDock-modeled SIRT2-**39** complex structure to reduce the steric hindrance between **39** and its nearby amino acid residues. To maintain the docked pose of **39**, we constrained the docked geometry of **39**, allowing the amino acid residues in SIRT2 to orient properly. The parameters used in the short MD run are described as follows: 10,000 steps of steepest-descent minimization using RMS gradient = 0.1 on SIRT2, followed by another 5,000 steps with conjugate-gradient minimization using RMS gradient = 0.05 on SIRT2; 5,000 steps for heating from 0 to 300 K; 50,000 steps for equilibration; and 1 ns for production, where the time interval for each step was 1 fs. The final snapshot of this short MD run was used as the initial SIRT2-**39** conformation for the follow-up MD simulation performed using AMBER 11.0.

When constructing the initial SIRT1-**39** and SIRT3-**39** complex structures, we processed structural alignment between SIRT2 and SIRT1 and between SIRT2 and SIRT3 according to the aforementioned implicit-water MD refined SIRT2-**39** structure to locate the region for accommodating **39**. The root-mean-square deviation (RMSD) value was 4.9 Å for the aligned SIRT1-**39** and SIRT2-**39** and 6.0 Å for the aligned SIRT3-**39** and SIRT2-**39**. The superposed SIRT2-**39** and SIRT1-**39** conformations and the superposed SIRT2-**39** and SIRT3-**39** conformations (not shown in this paper) suggested major structural discrepancies in their small domains, whereas their large domains exhibited favorable alignment.

The force-field parameters for the ligand were generated using the general AMBER force field by employing the Antechamber program.⁶⁹ The partial atomic charges for the ligand atoms were assigned using the AM-BCC protocol⁷⁰ after electrostatic potential calculations at the HF/6-31G* level. All hydrogen atoms of the three proteins were assigned using the LEaP module in consideration of ionizable residues set at their default protonation states at a neutral pH value. Each complex was immersed in a cubic box of the TIP3P water model.⁷¹ The size of the box was set such that the distance between the atoms in the studied complex and the wall was greater than 12 Å. Five, six, and seven Na⁺ ions were added to neutralize the SIRT1-**39**, SIRT2-**39**, and SIRT3-**39** complex systems, respectively. The solvated system was energy-minimized

through three stages, each employing 15,000 steps of the steepest descent algorithm and 15,000 steps of the conjugate-gradient algorithm with a nonbonded cutoff of 8.0 Å. At stage 1, the protein and **39** were restrained, enabling the added TIP3P water molecules to adjust to their proper orientations. At stage 2, the protein backbone was restrained to enable the amino acid side chains to find a superior way of accommodating **39**, especially for the manually formed SIRT1-**39**, SIRT2-**39**, and SIRT3-**39** systems. At stage 3, the entire solvated system was minimized without any restraint.

The MD simulations in this study were performed according to the standard protocol, which consists of gradual heating, density, equilibration, and production procedures in the isothermal isobaric ensemble (NPT, P = 1 atm, and T = 300 K) MD. A minimized solvated system was used as the starting structure for subsequent MD simulations. In the 500 ps heating procedure, the system was gradually heated from 0 to 300 K for 500 ps, followed by density at 300 K for 300 ps, and then constant equilibration at 300 K for 500 ps. After the equilibration procedure, the system underwent a 30 ns production procedure for conformation collection. The time step was set at 2 fs. Snapshots were taken at 10 ps intervals to record the conformation trajectory during the production MD stimulation. An 8 Å cutoff was applied to treat nonbonding interactions, such as short-range electrostatics and van der Waals interactions, and the particle-mesh-Ewald method was applied to treat long-range electrostatic interactions.⁷² The SHAKE algorithm⁷³ was used to limit all bonds containing hydrogen atoms to their equilibrium lengths. For structural and energetic analysis, we captured the trajectory in the final 5 ns (i.e., 500 conformation snapshots) for each complex system.

Binding Free Energy Calculations

MM/GBSA⁵⁹ is a popular approach for investigating the energetic contribution to protein-small molecule binding affinity. To compare **39** binding free energies in different SIRTs, MM/GBSA calculations were applied to the snapshots extracted from the final 5 ns of the MD trajectories. The binding free energy was computed for each molecular species, including complexes, ligands, and proteins, as the difference

$$\Delta G_{\text{binding}} = G_{\text{SIRT-39}} - [G_{\text{SIRT}} + G_{\text{39}}]$$

where

$$G_{\text{molecule}} = \langle E_{\text{MM}} \rangle + \langle G_{\text{solvation}}^{\text{polar}} \rangle + \langle G_{\text{solvation}}^{\text{nonpolar}} \rangle - TS,$$

$$\langle E_{\text{MM}} \rangle = \langle E_{\text{internal}} \rangle + \langle E_{\text{electrostatic}} \rangle + \langle E_{\text{vdW}} \rangle,$$

and

$$G_{\text{solvation}}^{\text{nonpolar}} = \gamma A + \beta.$$

$\langle \dots \rangle$ denotes the average for a set of structures extracted from a series of snapshots along an MD trajectory, and $\Delta G_{\text{binding}}$ is estimated from contributions of gas-phase energies i.e., $\langle E_{\text{MM}} \rangle$; solvation free energies, including polar and nonpolar terms; and entropies. Regarding gas-phase energies, E_{internal} includes the bond, angle, and torsional energies, and $E_{\text{electrostatic}}$ and E_{vdW} represent the electrostatic and van der Waals energies, respectively. The polar solvation, $G_{\text{solvation}}^{\text{polar}}$, is calculated using generalized Born model.⁵⁹ The nonpolar solvation term, $G_{\text{solvation}}^{\text{nonpolar}}$, is calculated with constants 0.00542 kcal mol⁻¹

\AA^2 for surface tension proportionality constant γ and 0.92 kcal mol^{-1} for the nonpolar free energy for a point solute β . The solvent accessible surface area, A , is varied according to the molecule and is calculated using a computer program. The entropy term, TS , arises from changes in degrees of freedom, including the translational, rotational, and vibrational terms of the solute molecules, and is estimated using the classical statistical thermodynamics approach. Conformational entropy was not included in our approach because it is computationally expensive.

Results and Discussion

Statistical Parameters of the CoMFA Model

The statistical parameters of the CoMFA model are summarized in Table 2. The $\text{ONC} = 5$ was recommended after a LOO cross-validated run yielded a value of $r^2 = 0.884$ and the subsequent non-cross-validated $R^2 = 0.992$ yielded a value higher than the criterion value of 0.6 required for a favorable model. Modelling using the test set to predict their pIC_{50} values with $R_{\text{test}}^2 = 0.804$ further ensured the predictive ability of the model built using the training set. The corresponding field contributions of steric and electrostatic are 63.2% and 36.8%, indicating the relatively higher influence of the steric field compared with that of the electrostatic field.

The pIC_{50} values predicted using the CoMFA model are listed in Table S1 (in supplementary material) alongside the experimentally observed pIC_{50} values and the residuals defined by the experimentally observed pIC_{50} values after the modelling-predicted pIC_{50} values were subtracted. The experimentally observed pIC_{50} values are plotted versus the modelling-predicted pIC_{50} values in Fig. 3. The residuals between the predicted and experimentally observed pIC_{50} values of the training set were between +0.209 and -0.115 for the training set and between +0.695 and -0.383 for the test set.

Table 2. Statistic results of CoMFA model

r^2	0.884
ONC	5
R^2	0.992
SEE	0.072
F	566.937
R_{test}^2	0.804
Contributions	
Steric	0.632
Electrostatic	0.368

^aAbbreviations used

r^2 : leave-one-out cross-validated correlation coefficient;
 ONC: optimum number of principal components;
 R^2 : non-cross-validated correlation coefficient (for training set);
 SEE: standard error of the estimate;
 F : F-ratio;
 R_{test}^2 : correlation coefficient of predicted test set pIC_{50} by model.

CoMFA Model Interpretation

In the steric-field contour map containing a background of **39**, as shown in Fig. 4A, a green contour, which prefers a bulky group to increase the designed inhibitor's activity, surrounds **39**'s fluorobenzene moiety, extending from the aniline of the 2-

anilinobenzamide core. Compounds **31–46** possessed such a ring moiety characterized by a long OCH_2CH_2 linkage rooted to the core and reaching the green contour and exhibited IC_{50} values (ranging from 0.57 to 3.4 μM) much lower than those of the other compounds studied in the series. However, large yellow contours that avert bulky groups can be classified as two regions. A set of yellow contours appeared on the upper right corner, implying that an extension on the para site relative to the aniline amino group is not preferred, as evidenced by **8–21** with IC_{50} values ranging from 17 to 93 μM . Another set of yellow contours on the lower right corner indicated that a short extension on the meta site, relative to the aniline amine group, was harmful to inhibitory activity, as proved by **1–7** and **22–29**, of which the IC_{50} values were between 24 and 100 μM .

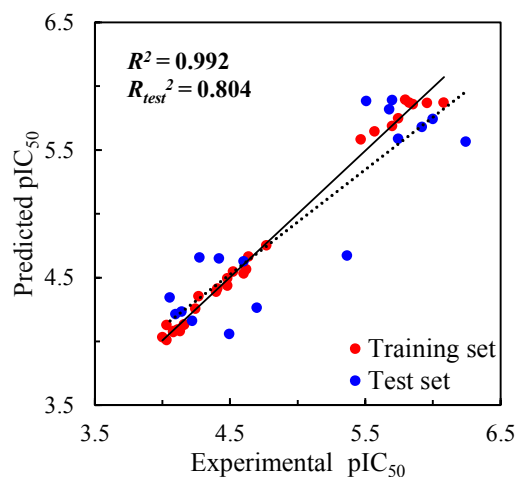


Fig. 3 CoMFA prediction for the training and test sets for SIRT2 inhibitory activities with the regression lines for the training set (solid line) and test set (dash line) predictions.

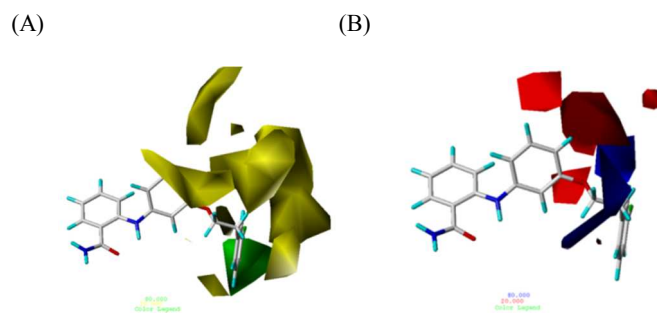


Fig. 4 Std* coeff contour maps of CoMFA model with **39**. (A) Steric fields: green/yellow contours indicate regions with bulky groups favorable/detrimental to the inhibitory activity. (B) Electrostatic fields: blue/red contours represent regions with electron-donating/withdrawing groups beneficial to the inhibitory activity.

Fig. 4B shows the electrostatic field, exhibiting **39** in the background, where blue and red contours represent electropositive and electronegative groups, respectively, that benefit activity. The blue contour in the background was

supported by a comparison between **3** (in which an electronegative $-CF_3$ group was in contact with this blue contour, resulting in a poorer IC_{50} value of 100 μM) and **4** (in which an $-OPh$ group bypassing this blue contour resulted in a superior IC_{50} value of 25 μM).

MD Simulations of Compound **39**-Bound SIRT Systems

MD simulations were performed for 30 ns to investigate the mode of **39** binding to the three SIRT isoforms and, thus, elucidate the selectivity for SIRT2 over SIRT1 and SIRT3. The RMSD from the initial structure was monitored to examine the dynamic stability of the complexes and plotted against time, as shown in Fig. 5. The magenta line in Fig. 5A denotes the RMSD for the amino acid backbone atoms throughout SIRT1-**39**, whereas the grey line signifies the backbone atoms near **39** bound in a sphere with a radius of 10 Å. The magenta line suggests that the complex was not stable at the early stage and after a conformational alternation the complex became stable at approximately 7 ns. Such a conformational alternation occurred outside the binding pocket because the grey line is relatively stable. The blue and grey lines in Fig. 5B for SIRT2-**39** showing almost the same trend in conformation variation indicate that the entire complex and the binding site region reached stability at approximately 6 ns. Fig. 5C shows that the structural mobility of the SIRT3-**39** complex was higher than that of the other two complexes, implying that **39** may not be suitable for SIRT3. The trajectory reached stable around 20 ns. We used the last 5 ns in subsequent structural and energetic analyses for the three complexes.

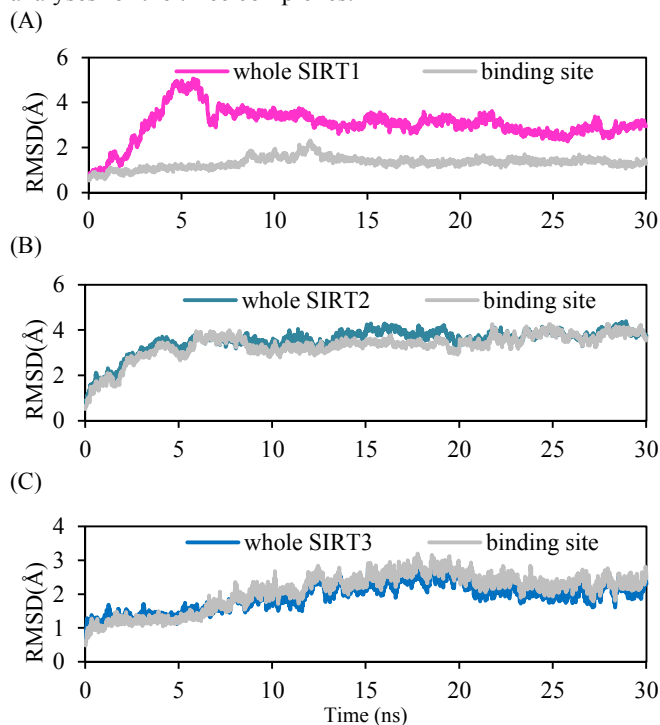


Fig. 5 RMSDs of heavy atoms of the protein and ligand in the entire complex or within the binding pocket for: (A) SIRT1-**39**, (B) SIRT2-**39**, and (C) SIRT3-**39** as a function of the simulation time.

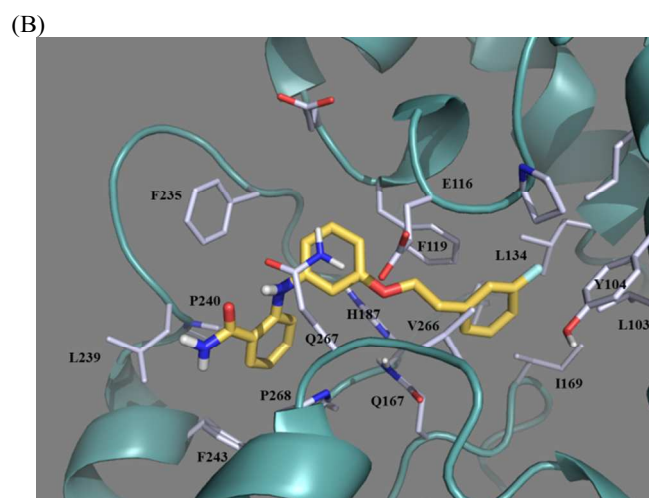
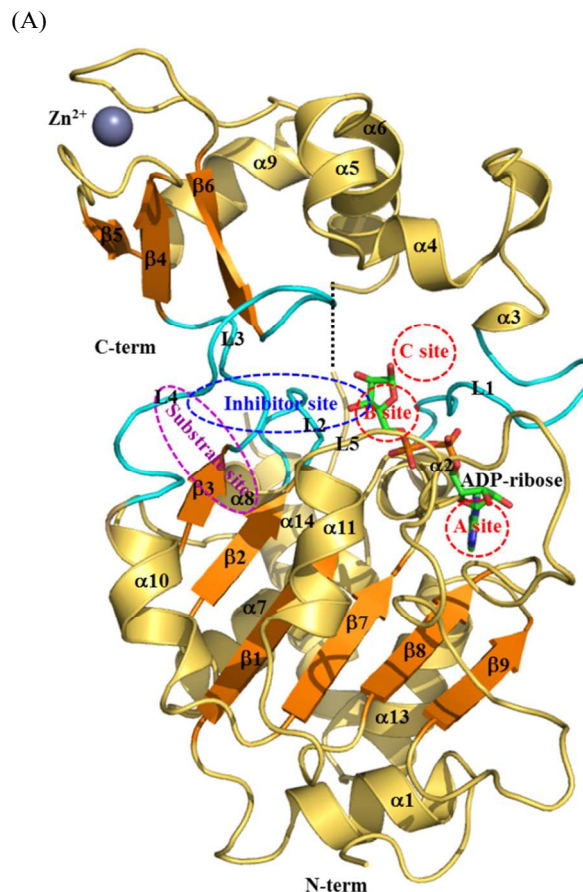


Fig. 6 Specification of binding sites in SIRT 2. (A) Overall structure of SIRT2 (based on PDB code: 3ZGV) showing the NAD⁺ site (divided into A, B, and C sites), peptide substrate binding site, and **39** binding site denoted as inhibitor site. (B) A close up view of predicted SIRT2-**39** binding mode.

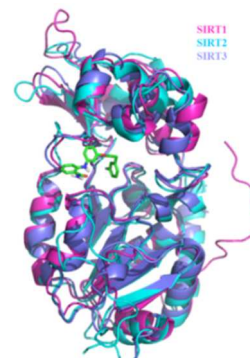
Fig. 6A shows the complex structure of human SIRT2 in complex with ADP-ribose (PDB code: 3ZGV) and contains labels denoting the **39** binding and substrate sites. The structural architecture of SIRT2 has two domains: a large domain and a small domain.^{74, 75} The large domain comprises six β -strands ($\beta 1$ - $\beta 3$ and $\beta 7$ - $\beta 9$) forming a parallel β -sheet and

six α -helices ($\alpha 1$, $\alpha 7$, $\alpha 8$, $\alpha 10$, $\alpha 11$, and $\alpha 13$) packed against the β -sheet. This large domain is in a Rossmann fold, which is present in various NAD(H)/NADP(H) binding enzymes. The small domain contains two structural modules: (i) a helical module, including $\alpha 3$ – $\alpha 6$, and (ii) a zinc-binding module, including $\alpha 9$ and $\beta 4$ – $\beta 6$ in an antiparallel β -sheet where the zinc ion is anchored by four conserved cysteine residues: C195, C200, C221, and C224. Linkage between the large domain and the small domain is achieved by three loops, including L1, which links $\alpha 2$ and $\alpha 3$; L3, which links $\beta 3$ and $\beta 4$; and L4, which links $\alpha 10$ and $\beta 6$. The NAD⁺ binding groove (i.e., the ADP-ribose binding site) in Fig. 6A, is usually divided into three regions: A site for accommodating the adenine ring, B site is for the nicotinamide ribose where deacetylation occurs, and C site, which, despite not being in contact with the NAD⁺, is for polarizing and hydrolyzing the NAD⁺ glycosidic bond for nicotinamide cleavage.⁷⁶ Compared with the free-state SIRT2 (PDB code: 1J8F),⁷⁵ the ADP-ribose-bound state of SIRT2 (PDB code: 3ZGV)⁶⁵ shows that L1 undergoes a remarkable conformational alternation upon ADP-ribose binding. In more detail, in the absence of the ADP-ribose, the L1 loop and $\alpha 3$ – $\alpha 6$ form a more compact helical module; whereas, upon ADP-ribose binding, L1 moves 25° downward to the large domain to clamp the bound ADP-ribose ligand.⁷³ Regarding the substrate binding site, a groove between $\alpha 10$ and $\alpha 11$ and above the parallel β -sheet created by $\beta 1$ and $\beta 2$ was proposed as ideal for a peptide substrate possessing an acetyl-lysine side chain oriented toward the B site for deacetylation. The predicted binding site of **39**, also shown in Fig. 6A, is spaciouly overlapped by the site for acetyl-lysine of the substrate, suggesting that the inhibition mechanism of the studied SIRT2 inhibitors is achieved through competition. It can be correlated to the RMSD result in Fig. 5B that SIRT2 does not undergo significant conformational alternation upon accommodating **39**.

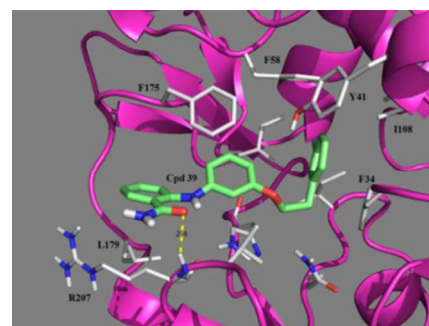
Fig. 6B shows a close-up view of the simulated binding mode of **39** within SIRT2 possessing a benzamide moiety oriented toward the entrance of the substrate binding groove and the extended phenyl ring moiety inserted into the B site. An intramolecular hydrogen bond exists between the amino-hydrogen atom and the amide-oxygen atom in **39** to maintain the relative orientation of the aniline and benzamide moieties. The binding pocket is mainly hydrophobic and surrounded by aromatic amino acid residues (F243, F235, F119, and Y104) and aliphatic amino acid residues (V266, L239, L134, and L103). In the large domain near the substrate entrance, P268 (on $\alpha 11$) and L239 (on L4) clamp the amino group of **39**. F243 (on $\alpha 10$) and F235 (on L4 that links $\beta 6$ and $\alpha 10$) encompass the benzamide moiety of **39** to provide π -stacking interaction where the separation distances between the ring centroids are 5.37 Å for F243-benzamide and 6.49 Å for F235-benzamide. F119 (on $\alpha 4$) faces the aniline and the extended phenyl-ring moieties of **39** with the separation distances between the ring centroids 4.53 and 5.71 Å, respectively. Y104 (at the junction of $\alpha 3$ and L1) and the long side chains of L103 (on L1) and L134 (on $\alpha 6$) surround the extended phenyl ring of **39**. V266 (on L5 connecting $\alpha 11$ and $\beta 7$ in the large domain) stabilizes the

linkage between the extended phenyl ring and the aniline moiety through van der Waals interaction, with the separation distance 5.37 Å between the centroid of V266's side chain and the phenyl ring's centroid. The only hydrophilic amino acid, E116 (adjacent to the beginning of $\alpha 4$), does not form any electrostatic interaction with **39**; instead, its negatively charged side chain forms a hydrogen bond with the backbone NH atom of Q267 (on L5 linking $\beta 7$ and $\alpha 11$) to lock the helical module and the large domain of SIRT2, possibly contributing a certain degree of stability to the SIRT2-**39** complex.

(A)



(B)



(C)

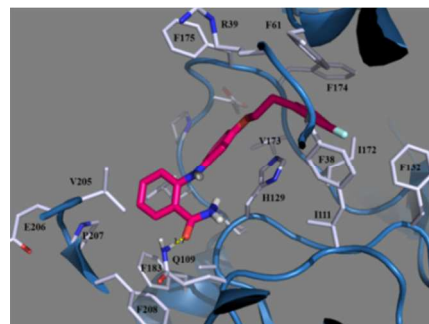


Fig. 7 Comparison of binding modes of **39**. (A) Superimposition of three SIRT-**39** complexes (color code: magenta for SIRT1-**39**, blue for SIRT2-**39**, and petrol for SIRT3-**39**) obtained by MD simulations in this work, (B) a close up view of predicted SIRT1-**39** binding mode, and (C) a close up view of predicted SIRT3-**39** binding mode.

The position of Q267 in our simulation data differed from that predicted by Suzuki and colleagues.⁵² Suzuki's model suggested that Q267 uses its side chain carbonyl-oxygen atom and amino-hydrogen atom to form two hydrogen bonds with the amino-hydrogen atom and amide-oxygen atom of **10**, respectively.⁵² Such a discrepancy may have resulted from the extended phenyl ring moiety existing in para or meta positions relative to the amino group in **10** or **39**. Furthermore, Suzuki's molecular docking adopted an Hst2-based homology modeled on SIRT2 structures, whereas we used a human ADP-ribose-bound SIRT2 structure in which Q267 is secured by its neighboring Q167, Q116, E235, and V6. Because the Q267 in our model cannot interact with **39**, the docking result showed that **39** prefers a docking position that is slightly outward compared to Suzuki's prediction.

A comparison between our MD simulation on SIRT-**39** and the QSAR models revealed the following agreements. First, the yellow steric-disfavoured contour in Fig. 4A on the para position of the aniline moiety relative to the amine group can be related to the bulky side chain of F119. In other words, a modification on this corner would clash with F119. However, the green steric-favoured contour in Fig. 4A can be correlated with the empty space at the nearby the C site. The red contour in Fig. 4B, which prefers a negatively charged modification, can be related to the basic side chain of H187, of which the closeness enhances the electrostatic attraction.

Fig. 7A shows superposed snapshots of the three SIRT-**39** complexes, indicating the RMSD value for SIRT1-**39** relative to SIRT2-**39** to be 4.90 Å, that of SIRT3-**39** relative to SIRT2-**39** to be 6.01 Å, and that of SIRT1-**39** relative to SIRT3-**39** to be 4.45 Å. In contrast to the diverse small domains of the three SIRTs, the large domains among these three complexes align favourably. Fig. 7B shows a model of the SIRT1-**39** complex, in which **39** uses its amino-oxygen atom to form a hydrogen bond with the amine-hydrogen atom of the backbone of R207, exhibiting 88% hydrogen bond occupancy in the entire 30 ns MD simulation. R207 is located at the beginning of α 11 (analogous to SIRT2 P268). R207 and L179 (at the beginning of L4 and analogous to SIRT2 L239) reside at the substrate-binding entrance of the large domain. The binding pocket of SIRT1 is hydrophobic and is composed of several aromatic amino acid residues, including F175 (on L4 and analogous to SIRT2 F235), which stabilizes the aniline ring (with a separation distance of 3.96 Å between two ring moieties' centroids); Y41 (on α 3 and analogous to SIRT2 Y104), which stabilizes the extended phenyl ring (with a separation distance of 9.00 Å between two ring moieties' centroids); F58 (on α 4 and analogous to F119), which stabilizes both the aniline ring (with a separation distance of 7.38 Å between two ring moieties' centroids) and the extended phenyl ring (with a separation distance of 7.31 Å between two ring moieties' centroids); and F34 (on L1), which stabilizes the extended phenyl ring (with a separation distance of 4.99 Å between two ring moieties' centroids). These van der Waals interactions are provided by the upper region of SIRT1, except F34 is from L1 on the lateral side, whereas the electrostatic interaction comes from the large

domain. Table 3 lists the binding free energies calculated using the MM/GBSA approach. SIRT1 and SIRT2 hold almost the same van der Waals interactions toward **39** (-48.08 and -50.21 kcal/mol for SIRT1-**39** and SIRT2-**39**, respectively), and SIRT1 carries a markedly higher electrostatic interaction (-14.48 vs. -1.57 kcal/mol) because of the stable hydrogen bond of R207. However, a higher polar solvation instability at SIRT1-**39**, possibly caused by the reduced solvent accessibility of R207 and N178 upon SIRT1-**39** formation, causes the ΔG_{bind} of SIRT1-**39** (-39.20 kcal/mol) to be lower than that of SIRT2-**39** (-43.05 kcal/mol), confirming the experimentally determined IC_{50} values.

The orientation of **39** in SIRT3-**39**, as shown in Fig. 7C, is similar to that in the other two complexes. The side chain amine hydrogen atom of Q109 (on the β 2) forms a hydrogen bond with the amino-hydrogen atom of **39** with 58% occupancy in the last 10 ns in the whole 30 ns MD duration. Accordingly, the ΔG_{elec} term of SIRT3-**39** is between that of SIRT1-**39** and SIRT2-**39**. F174 (on L4 and analogous to SIRT1 F174 and SIRT2 F234, even though these two residues do not face any ring of **39**) toward the extended phenyl ring (with a separation distance of 5.81 Å between two ring moieties' centroids), F61 (on the C-terminus of α 4) toward the extended ring (with a separation distance of 4.79 Å between two ring moieties' centroids), and F38 (on L1) toward the extended ring (with a separation distance of 6.73 Å between two ring moieties' centroids). Overall, the electrostatic interactions come from the large domain, and the van der Waals interactions are either from the helical module or loops. Compared with the two aforementioned SIRT-**39** complexes, **39** is more exposed to the solvent when binding to SIRT3, and therefore, its van der Waals contribution is the smallest, as shown in the ΔG_{vdw} column. The ΔG_{bind} for SIRT3-**39** (-34.59 kcal/mol) and SIRT2-**39** (-43.05 kcal/mol) correspond to their >300 and 0.57 μM IC_{50} values, as determined by Suzuki and colleagues.⁵²

According to the structural and energetic analyses conducted in this study, SIRT1 binds to **39** more strongly than SIRT3 does, although both SIRT1-**39** and SIRT3-**39** exhibit inhibitory activities at concentrations >300 μM . Compared with the binding pocket in SIRT1 and SIRT2, the binding pocket in SIRT3 is larger and, thus, **39** is loosely bound therein. However, two hydrogen bonds, although in low hydrogen bond occupancies, form between SIRT3 and **39**, and, therefore, any further modification on the same series of inhibitors should avoid these hydrogen bond formations to discriminate SIRT3.

Disch and colleagues recently identified a series of pan-SIRT inhibitors in a scaffold of thieno[3,2-d]pyrimidine-6-carboxamides exhibiting nanomolar inhibition potency toward SIRT1, SIRT2, and SIRT3.⁷⁷ The crystal structure of SIRT3 bound with **11C** in described by Disch suggests that such pan-SIRT inhibitors occupy a binding pocket that is similar to that used by the aniline and extended phenol moieties of **39** herein. Accordingly, the selectivity of the 2-anilinobenzamide series of SIRT2 inhibitors should rely on the modification of a benzoamide side that exhibits differential binding behaviours among SIRT1, SIRT2, and SIRT3.

Conclusion

This study applied CoMFA to investigate a series of 2-anilinobenzamide derivatives and, thus, determine the structural requirements essential to fit the NAD⁺-dependent histone deacetylase SIRT2. In addition, molecular docking and MD simulations were used to investigate the binding modes of **39**, which demonstrated a higher inhibitory potency for SIRT2 than for SIRT1 and SIRT3 in Suzuki's selectivity assay.⁵² As concluded in Fig. 8, the steric field generated by the CoMFA suggested that an extended modification rooted on the meta position of the aniline moiety can form π stacking with the SIRT2 F119, whereas a para extension can conflict with F119, as indicated by the molecular docking result. The binding pocket in SIRT2 is mainly hydrophobic and encompassed by numerous aromatic amino acids (Y104, F119, F243, and F235) and aliphatic amino acids (L103, L134, L239, and V266). Moreover, a great portion of the benzamide plane is clamped by L239 and P268 located on α 10 and α 11. In summary, **39** is stabilized by the large domain and the helical module of SIRT2. By contrast, except for R207 from the large domain, which forms a hydrogen bond with **39**, SIRT1 exhibits affinity toward **39** from the helical module. Regarding SIRT3, its binding pocket is slightly larger than those of SIRT1 and SIRT2 and accordingly exhibits the lowest affinity, as verified according to the ΔG_{bind} term and a loosely binding mode in the structural analysis. Because both SIRT1 and SIRT3 exhibit the potential to form hydrogen bonds with **39**, further modifications for enhancing the preference of **39** for SIRT2 should avoid hydrogen bond donors or acceptors oriented toward SIRT1 R207 and SIRT3 Q109. These computational results will benefit the further development of selective SIRT2 inhibitors.

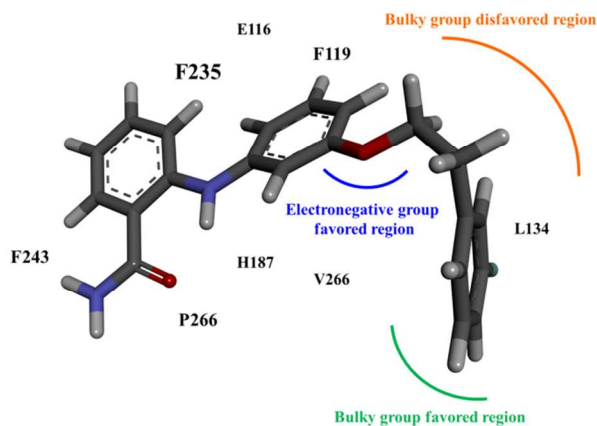


Fig. 8 Concluded remarks of the CoMFA model for SIRT2 inhibitors with a 2-anilinobenzamide scaffold.

Acknowledgement

This work was supported by the National Science Council of Taiwan (NSC 102-2113-M-390-007-MY2).

Notes and references

^a Department of Life Science, National University of Kaohsiung, Taiwan.

^b Division of Urology, Department of Surgery, Kaohsiung Veterans General Hospital, Kaohsiung, Taiwan.

† All correspondence should be addressed to Chia-Ning Yang, PhD

Tel: 886-7-5919717

Fax: 886-75919404

E-mail: cnyang@nuk.edu.tw

Address: No. 700, Kaohsiung University Road, Nan-Tzu District 811, Kaohsiung, Taiwan

Electronic Supplementary Information (ESI) available: [S1 table]. See DOI: 10.1039/b000000x/

1. P. Hu, S. L. Wang and Y. K. Zhang, *Journal of the American Chemical Society*, 2008, **130**, 16721-16728.
2. G. Blander and L. Guarente, *Annual Review of Biochemistry*, 2004, **73**, 417-435.
3. R. Marmorstein, *Biochem Soc Trans*, 2004, **32**, 904-909.
4. J. M. Denu, *Curr Opin Chem Biol*, 2005, **9**, 431-440.
5. C. W. Anthony A. Sauve, Vern L. Schramm, and Jef D. Boek, *Annual Review of Biochemistry*, 2006, **75**, 435-465.
6. M. A. D. C.H. Westphal, L. Guarente, *Trends in Biochemical Sciences*, 2007, **32**, 555-590.
7. K. S. Hiroyasu Yamamoto, and Johan Auwerx, *Molecular Endocrinology*, 2007, **21**, 1745-1755.
8. D. A. S. Philipp Oberdoerffer, *Nature Reviews Molecular Cell Biology*, 2007, **8**, 692-702.
9. D. Moazed, *Current Opinion in Cell Biology*, 2001, **13**, 232-238.
10. M. M. C. Susan M. Gasser, *Gene*, 2001, **279**, 1-16.
11. S. Hekimi and L. Guarente, *Science*, 2003, **299**, 1351-1354.
12. A. Brunet, L. B. Sweeney, J. F. Sturgill, K. F. Chua, P. L. Greer, Y. X. Lin, H. Tran, S. E. Ross, R. Mostoslavsky, H. Y. Cohen, L. S. Hu, H. L. Cheng, M. P. Jedrychowski, S. P. Gygi, D. A. Sinclair, F. W. Alt and M. E. Greenberg, *Science*, 2004, **303**, 2011-2015.
13. M. C. Motta, N. Divecha, M. Lemieux, C. Kamel, D. Chen, W. Gu, Y. Bultsma, M. McBurney and L. Guarente, *Cell*, 2004, **116**, 551-563.
14. V. J. Starai, H. Takahashi, J. D. Boeke and J. C. Escalante-Semerena, *Current Opinion in Microbiology*, 2004, **7**, 115-119.
15. S. Gottlieb and R. E. Esposito, *Cell*, 1989, **56**, 771-776.
16. M. Kaeberlein, M. McVey and L. Guarente, *Genes Dev*, 1999, **13**, 2570-2580.
17. S. J. Lin, P. A. Defossez and L. Guarente, *Science*, 2000, **289**, 2126-2128.
18. J. Luo, A. Y. Nikolaev, S. Imai, D. Chen, F. Su, A. Shiloh, L. Guarente and W. Gu, *Cell*, 2001, **107**, 137-148.
19. H. A. Tissenbaum and L. Guarente, *Nature*, 2001, **410**, 227-230.
20. H. Vaziri, S. K. Dessain, E. Ng Eaton, S. I. Imai, R. A. Frye, T. K. Pandita, L. Guarente and R. A. Weinberg, *Cell*, 2001, **107**, 149-159.
21. M. A. McMurray and D. E. Gottschling, *Science*, 2003, **301**, 1908-1911.
22. M. Biel, V. Wascholowski and A. Giannis, *Angew Chem Int Ed Engl*, 2005, **44**, 3186-3216.
23. B. Heltweg, T. Gattbonton, A. D. Schuler, J. Posakony, H. Li, S. Goehle, R. Kollipara, R. A. Depinho, Y. Gu, J. A. Simon and A. Bedalov, *Cancer Res*, 2006, **66**, 4368-4377.

24. T. F. Outeiro, E. Kontopoulos, S. M. Altmann, I. Kufareva, K. E. Strathearn, A. M. Amore, C. B. Volk, M. M. Maxwell, J. C. Rochet, P. J. McLean, A. B. Young, R. Abagyan, M. B. Feany, B. T. Hyman and A. G. Kazantsev, *Science*, 2007, **317**, 516-519.
25. Y. Itoh, T. Suzuki and N. Miyata, *Curr Pharm Des*, 2008, **14**, 529-544.
26. J. C. Milne and J. M. Denu, *Curr Opin Chem Biol*, 2008, **12**, 11-17.
27. P. Moretti, K. Freeman, L. Coodly and D. Shore, *Genes Dev*, 1994, **8**, 2257-2269.
28. A. Hecht, T. Laroche, S. Strahl-Bolsinger, S. M. Gasser and M. Grunstein, *Cell*, 1995, **80**, 583-592.
29. A. Hecht, S. Strahl-Bolsinger and M. Grunstein, *Nature*, 1996, **383**, 92-96.
30. D. Moazed, A. Kistler, A. Axelrod, J. Rine and A. D. Johnson, *Proc Natl Acad Sci U S A*, 1997, **94**, 2186-2191.
31. S. Strahl-Bolsinger, A. Hecht, K. Luo and M. Grunstein, *Genes Dev*, 1997, **11**, 83-93.
32. W. Shou, J. H. Seol, A. Shevchenko, C. Baskerville, D. Moazed, Z. W. Chen, J. Jang, H. Charbonneau and R. J. Deshaies, *Cell*, 1999, **97**, 233-244.
33. A. F. Straight, W. Shou, G. J. Dowd, C. W. Turck, R. J. Deshaies, A. D. Johnson and D. Moazed, *Cell*, 1999, **97**, 245-256.
34. E. Langley, M. Pearson, M. Farettta, U. M. Bauer, R. A. Frye, S. Minucci, P. G. Pelicci and T. Kouzarides, *EMBO J*, 2002, **21**, 2383-2396.
35. E. Michishita, J. Y. Park, J. M. Burneskis, J. C. Barrett and I. Horikawa, *Mol Biol Cell*, 2005, **16**, 4623-4635.
36. J. Smith, *Trends Cell Biol*, 2002, **12**, 404-406.
37. B. J. North, B. L. Marshall, M. T. Borra, J. M. Denu and E. Verdin, *Mol Cell*, 2003, **11**, 437-444.
38. T. Inoue, M. Hiratsuka, M. Osaki and M. Oshimura, *Cell Cycle*, 2007, **6**, 1011-1018.
39. T. Shi, F. Wang, E. Stieren and Q. Tong, *J Biol Chem*, 2005, **280**, 13560-13567.
40. C. Argmann and J. Auwerx, *Cell*, 2006, **126**, 837-839.
41. N. Ahuja, B. Schwer, S. Carobbio, D. Waltregny, B. J. North, V. Castronovo, P. Maechler and E. Verdin, *J Biol Chem*, 2007, **282**, 33583-33592.
42. M. A. Holbert and R. Marmorstein, *Curr Opin Struct Biol*, 2005, **15**, 673-680.
43. C. Corminboeuf, P. Hu, M. E. Tuckerman and Y. Zhang, *J Am Chem Soc*, 2006, **128**, 4530-4531.
44. L. J. Juan, W. J. Shia, M. H. Chen, W. M. Yang, E. Seto, Y. S. Lin and C. W. Wu, *J Biol Chem*, 2000, **275**, 20436-20443.
45. A. Ito, Y. Kawaguchi, C. H. Lai, J. J. Kovacs, Y. Higashimoto, E. Appella and T. P. Yao, *EMBO J*, 2002, **21**, 6236-6245.
46. M. A. Gluzak, N. Sengupta, X. Zhang and E. Seto, *Gene*, 2005, **363**, 15-23.
47. S. Sakkiah, Krishnamoorthy, N., Gajendrarao, P., Thangapandian, S., Lee, Y., et al., *Bulletin of the Korean Chemical Society*, 2009, **30**, 1152-1156.
48. A. Vaquero, M. B. Scher, D. H. Lee, A. Sutton, H. L. Cheng, F. W. Alt, L. Serrano, R. Sternglanz and D. Reinberg, *Genes Dev*, 2006, **20**, 1256-1261.
49. P. H. Kiviranta, J. Leppanen, V. M. Rinne, T. Suuronen, O. Kyrylenko, S. Kyrylenko, E. Kuusisto, A. J. Tervo, T. Jarvinen, A. Salminen, A. Poso and E. A. Wallen, *Bioorg Med Chem Lett*, 2007, **17**, 2448-2451.
50. P. H. Kiviranta, H. S. Salo, J. Leppanen, V. M. Rinne, S. Kyrylenko, E. Kuusisto, T. Suuronen, A. Salminen, A. Poso, M. Lahtela-Kakkonen and E. A. Wallen, *Bioorg Med Chem*, 2008, **16**, 8054-8062.
51. J. Trapp, A. Jochum, R. Meier, L. Saunders, B. Marshall, C. Kunick, E. Verdin, P. Goekjian, W. Sippl and M. Jung, *J Med Chem*, 2006, **49**, 7307-7316.
52. T. Suzuki, M. N. Khan, H. Sawada, E. Imai, Y. Itoh, K. Yamatsuta, N. Tokuda, J. Takeuchi, T. Seko, H. Nakagawa and N. Miyata, *J Med Chem*, 2012, **55**, 5760-5773.
53. S. Karkola, A. Lilienkampf and K. Wahala, *ChemMedChem*, 2008, **3**, 461-472.
54. D. Li, M. S. Liu, B. Ji, K. Hwang and Y. Huang, *J Chem Phys*, 2009, **130**, 215102.
55. R. T. Shenoy, S. F. Chowdhury, S. Kumar, L. Joseph, E. O. Purisima and J. Sivaraman, *J Med Chem*, 2009, **52**, 6335-6346.
56. S. G. Estacio, R. Moreira and R. C. Guedes, *J Chem Inf Model*, 2011, **51**, 1690-1702.
57. Y. Yang, Y. Shen, H. Liu and X. Yao, *J Chem Inf Model*, 2011, **51**, 3235-3246.
58. R. D. Cramer, D. E. Patterson and J. D. Bunce, *J Am Chem Soc*, 1988, **110**, 5959-5967.
59. A. Onufriev, D. Bashford and D. A. Case, *Proteins*, 2004, **55**, 383-394.
60. *Sybyl 8.1*, Tripos International, St. Louis.
61. D. A. D. Case, T. A.; Cheatham, I., T.E.; Simmerling, C. L.; Wang, J.; Duke, R. E.; Luo, R.; Walker, R. C.; Zhang, W.; Merz, K. M.; Roberts, B.; Wang, B.; Hayik, S.; Roitberg, A.; Seabra, G.; Kolosváry, I.; Wong, K. F.; Paesani, F.; Vanicek, J.; Liu, J.; Wu, X.; Brozell, S. R.; Steinbrecher, T.; Gohlke, H.; Cai, Q.; Ye, X.; Wang, J.; Hsieh, M.-J.; Cui, G.; Roe, D. R.; Mathews, D. H.; Seetin, M. G.; Sagui, C.; Babin, V.; Luchko, T.; Gusarov, S.; Kovalenko, A.; Kollman, P. A. AMBER, 11; University of California: San Francisco, 2010., 2010.
62. Y. Duan, C. Wu, S. Chowdhury, M. C. Lee, G. Xiong, W. Zhang, R. Yang, P. Cieplak, R. Luo, T. Lee, J. Caldwell, J. Wang and P. Kollman, *J Comput Chem*, 2003, **24**, 1999-2012.
63. V. Hornak, R. Abel, A. Okur, B. Strockbine, A. Roitberg and C. Simmerling, *Proteins*, 2006, **65**, 712-725.
64. X. Zhao, D. Allison, B. Condon, F. Zhang, T. Gheyi, A. Zhang, S. Ashok, M. Russell, I. MacEwan, Y. Qian, J. A. Jamison and J. G. Luz, *J Med Chem*, 2013, **56**, 963-969.
65. S. Moniot, M. Schutkowski and C. Steegborn, *J Struct Biol*, 2013, **182**, 136-143.
66. G. T. Nguyen, S. Schaefer, M. Gertz, M. Weyand and C. Steegborn, *Acta Crystallogr D Biol Crystallogr*, 2013, **69**, 1423-1432.
67. *Discovery Studio Modeling Environment* Accelrys Software Inc, 2012.
68. S. N. Rao, M. S. Head, A. Kulkarni and J. M. LaLonde, *J Chem Inf Model*, 2007, **47**, 2159-2171.
69. J. Wang, W. Wang, P. A. Kollman and D. A. Case, *J Mol Graph Model*, 2006, **25**, 247-260.

70. A. Jakalian, D. B. Jack and C. I. Bayly, *J Comput Chem*, 2002, **23**, 1623-1641.
71. J. C. William L. Jorgensen, Jeffrey D. Madura, Roger W. Impey and Michael L. Klein, *The Journal of Chemical Physics*, 1983, **79**, 926.
72. T. Y. Darden, D.; Pedersen, L., *The Journal of Chemical Physics*, 1993, **98**, 10089.
73. G. C. Jean-Paul Ryckaert, Herman J.C Berendsen, *Journal of Computational Physics*, 1977, **23**, 327-341.
74. S. Moniot, M. Schutkowski and C. Steegborn, *J Struct Biol*, **182**, 136-143.
75. M. S. Finnin, J. R. Donigian and N. P. Pavletich, *Nat Struct Biol*, 2001, **8**, 621-625.
76. R. N. Duttall and L. Pillus, *Cell*, 2001, **105**, 161-164.
77. J. S. Disch, G. Evindar, C. H. Chiu, C. A. Blum, H. Dai, L. Jin, E. Schuman, K. E. Lind, S. L. Belyanskaya, J. Deng, F. Coppo, L. Aquilani, T. L. Graybill, J. W. Cuzzo, S. Lavu, C. Mao, G. P. Vlasuk and R. B. Perni, *J Med Chem*, 2013, **56**, 3666-3679.